

A Remarkable Auroral Event on Jupiter Observed in the Ultraviolet with the Hubble Space Telescope

J. C. Gérard,* D. Grodent, R. Prangé, J. H. Waite, G. R. Gladstone, V. Dols, F. Paresce, A. Storrs, L. Ben Jaffel, K. A. Franke

Two sets of ultraviolet images of the Jovian north aurora were obtained with the Faint Object Camera on board the Hubble Space Telescope. The first series shows an intense discrete arc in near corotation with the planet. The maximum apparent molecular hydrogen emission rate corresponds to an electron precipitation of ~ 1 watt per square meter, which is about 30,000 times larger than the solar heating by extreme ultraviolet radiation. Such a particle heating rate of the auroral upper atmosphere of Jupiter should cause a large transient temperature increase and generate strong thermospheric winds. Twenty hours after initial observation, the discrete arc had decreased in brightness by more than one order of magnitude. The time scale and magnitude of the change in the ultraviolet aurora leads us to suggest that the discrete Jovian auroral precipitation is related to large-scale variations in the current system, as is the case for Earth's discrete aurorae.

The first observations of the ultraviolet (UV) aurora on Jupiter were obtained by the UV spectrometer (UVS) on board the Voyager 1 and 2 spacecraft in 1979 (1–3). Data accumulated since 1980 with the UV spectrograph on the International Ultraviolet Explorer (IUE) satellite (4) have been used to indirectly characterize the main features of the morphological and brightness distribution of the aurora. From these early observations, some information was derived on its temporal behavior. Livengood *et al.* (4) analyzed 10 years of IUE data and found that the average observed auroral brightness profile was generally stable within a factor of about 2 to 3. The lack of spatial resolution of these nonimaging instruments did not allow the determination of whether morphological changes (in auroral shape or latitude) were associated with the brightness variations (4, 5). Some morphological differences were observed in 1992 on two Hubble Space Telescope (HST) Faint Object Camera (FOC) images (6) with nearly identical central meridian longitudes separated by about 3 days. However, in this case, both the maximum local brightness and the integrated radiated power showed little variation. The question of temporal variability is of major importance in under-

standing the origin and the acceleration mechanisms of the auroral particles exciting the Jovian UV aurora.

Basic differences exist between the magnetospheres of Jupiter and the Earth. The Earth's magnetosphere dynamics, controlled by the solar wind dynamo, organize auroral processes in a local time frame of reference with peak activity in the midnight sector. These processes take place on magnetic field lines from the central to distant plasma sheet in the nightside magnetotail. By contrast, the much more extensive Jovian magnetosphere is in quasi-corotation with the planet up to distances of about 20 Jovian radii. This feature explains why the UVS experiment on board Voyager (3) did not detect any significant day-night variation.

In July 1993, two series of three HST FOC images, each of the UV aurora, were taken nearly 20 hours apart to investigate the question of temporal variability. The filter isolated a 20-nm-wide region centered on 153 nm (7), which is dominated by the emission of the molecular hydrogen Lyman bands (H_2 Lyman) and the continuum. The relevant parameters of the observations are specified in Table 1.

Unexpectedly, the first series of exposures recorded a very bright auroral event that gave rise to a FOC count level about four times higher than any previous observations made with the same instrumental configuration. Nearly parallel spectrographic measurements made with the IUE (8) reveal that the emitted UV auroral radiation reached the second highest level recorded in over 12 years of IUE Jovian auroral observations. In the first exposure of the first series (I1) (Fig. 1A), a bright but

longitudinally limited portion of the auroral arc is visible near the approaching (dawn) limb of the planet. In the third exposure (I3) (Fig. 1B), the bright arc is considerably more extended in longitude. A comparison of the location of the emission morphology on the two exposures (9) shows that the entire pattern is in quasi-corotation with the planet. However, the leading edge of the bright arc is shifted to smaller longitudes by $\sim 52^\circ$, which is less than the 65° of planetary rotation. This slippage may be caused by a temporal brightness change along the auroral oval over the 107 min separating the two images.

The quasi-corotation demonstrates the predominantly longitudinal control of the auroral emission of Jupiter already suggested by the first FOC images at the Lyman α frequency, obtained in 1992, (10) and by years of IUE observations (4). The aurora has an uncertain brightness distribution along the auroral oval and may have a local time dependence as well as a longitude dependence. We also expect these H_2 Lyman emissions to be considerably brighter near the limb (11). For example, the apparent brightness near the limb is expected to be about eight times brighter than an identical aurora would be on the central meridian at a latitude of $60^\circ N$.

In the background-subtracted versions of images I2 and W1 (Fig. 2, A and B, respectively), the bright arc seen in Fig. 1A stretches from a latitude of $60^\circ N$ and a system III longitude (λ_{III}) of 180° to $\sim 70^\circ N$ on the dawn limb. A second, weaker spot of emission extends along the central meridian. Weak, diffuse emission fills the entire polar cap and reaches $\sim 50^\circ N$ near $\lambda_{III} = 190^\circ$. The brightest pixels correspond to a count rate of ~ 13 counts per pixel. This level is higher than previous HST FOC observations (6, 12, 13), which typically reached 2 to 4 counts per pixel above the disk background for similar exposure times. Converted into an apparent emission rate, the most intense parts of the auroral arcs in images I1, I2, and I3 reach ~ 3.6 megarayleighs (1 MR = 10^{12} photons per square centimeter per second) of H_2 Lyman

Table 1. Main characteristics of the HST FOC auroral observations. Abbreviations: UT, universal time; λ , wavelength; CML, central meridian longitude; NUV, near ultraviolet.

Date	UT	Central λ (nm)	CML (degrees)	Image
17 July	00:47	210	51	NUV
	02:21	153	108	I1
	03:48	153	160	I2
	04:08	153	172	I3
18 July	23:16	153	146	W1
	00:41	153	198	W2
	01:01	153	210	W3

J. C. Gérard, D. Grodent, V. Dols, Laboratoire de Physique Atmosphérique et Planétaire, Institut d'Astrophysique, Université de Liège, Belgium.

R. Prangé, Institut d'Astrophysique Spatiale and Institut d'Astrophysique de Paris, Université de Paris Sud, Orsay, France.

J. H. Waite, G. R. Gladstone, K. A. Franke, Southwest Research Institute, San Antonio, TX, 78228-0570, USA. F. Paresce and A. Storrs, Space Telescope Science Institute, Baltimore, MD 21218, USA.

L. B. Jaffel, Institut d'Astrophysique de Paris, France.

*To whom correspondence should be addressed.

emission, equivalent to ~ 6 MR of total H_2 emission (14).

Figure 2B illustrates the dramatic change that occurred during about two Jovian rotations. The bright arc previously seen at $\lambda_{III} > 180^\circ$ faded to a much weaker zone of inhomogeneous emission with a maximum near $60^\circ N$, $\lambda_{III} = 200^\circ$. Table 2 shows a comparison of the total power radiated in H_2 Lyman in images I2 and W1 and the maximum count rates in both exposures. The peaks of the auroral emission are in a ratio of nearly 8 to 1. However, the brightest part of the intense arc in Fig. 2A maps into a weak zone of ~ 1 count per pixel, indicating a drop to 1/13 of the local emission rate.

A global view of the auroral morphology and its variation during the event is best given by composite polar orthographic projections of images I1, I2, and I3 (Fig. 2C) and W1, W2, and W3 (Fig. 2D); they illustrate how the overall decrease in emission affected the morphology of the emission. The bright aurora observed in the first group of images (Fig. 2C) lies close to but not along the oval described by the footprint of the magnetic field lines crossing the equatorial plane at 30 Jovian radii (R_J). Gérard *et al.* (12) mapped the aurora observed over a complete Jovian rotation and found that a better fit can be obtained by shifting the center of the model oval by a few degrees. The leading edge of the bright emission lies near $\lambda_{III} = 180^\circ$, although a weaker extension is observed up to 165° . A secondary weaker alignment is seen along the 160° meridian, extending from $62^\circ N$ up to the limit of visibility. Dimmer unstructured aurora is visible inside and outside the discrete emission. It reaches an equatorward limit of $\sim 50^\circ N$ at $\lambda_{III} = 180^\circ$ at the 1σ threshold applied to the individual images. The corresponding projection 20 hours later (Fig. 2D) shows, in agreement with Fig. 2B, considerable brightness variations, but the morphology is reminiscent of Fig. 2C. A weak emission band is still present parallel to and outside of the 30 R_J oval at $\lambda_{III} > 180^\circ$. These features lead to the conclusion that the bright auroral arc already observed previously in the sector $\lambda_{III} > 180^\circ$ overlaid a diffuse auroral region that remained nearly invariant in brightness throughout the event.

Table 2 lists the estimated total radiated power over the half hemisphere facing the Earth derived from both I2 and W1. Using an energy conversion of ~ 7 for electron deposition (assuming that the auroral particles are energetic electrons) in a H_2 atmosphere (15–17), we find that the 6 MR of total H_2 emission correspond to a local flux of $\sim 1 W m^{-2}$ and a total radiated power of $10^{12} W$. The input of such a high energy flux must considerably perturb the energy

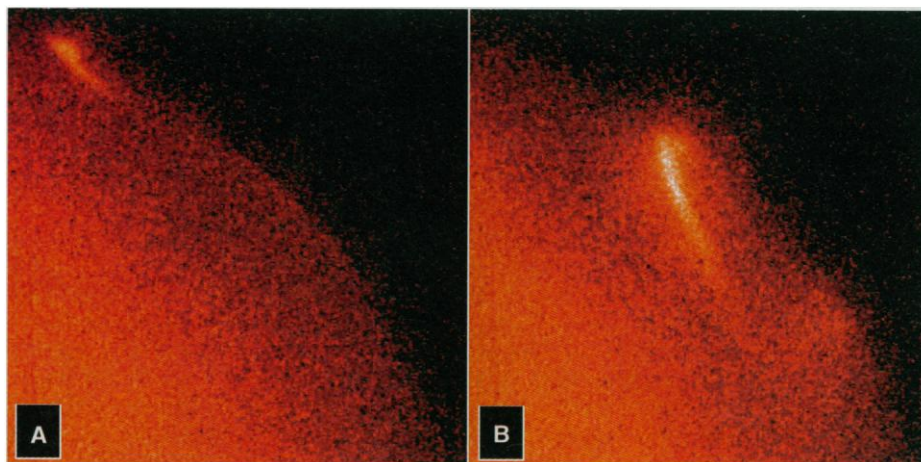


Fig. 1. Images of the Jovian aurora obtained at a wavelength of 153 nm with the HST FOC. The brightness of the disk background from solar UV radiation scattered by the atmosphere decreases from the mid-latitudes (lower left) to the polar region. The planetary limb is visible against dark space. (A) The first image of the first sequence (exposure I1). The aurora is visible near the limb and forms an ansa or loop near the (astronomical) eastern edge of the oval. (B) The third image (exposure I3) shows how the auroral distribution evolved in the 107 min separating the two exposures.

balance and the temperature profile of the Jovian upper atmosphere. As energetic electrons interact with the hydrogen gas by elastic and inelastic collisions, a large fraction of the energy input is converted into local gas heating. The consequences of an electron power input of $\sim 1 W m^{-2}$ can be crudely estimated with simple one-dimensional (1D) energy degradation and energy balance models (16, 18).

Because no direct information on the energy distribution of the auroral particles is available, we base our estimates on the HST spectroscopy observations of Trafton *et al.* (19) with a corresponding spectral power index of -4 and a low-energy cutoff at 22 keV. Two situations may be analyzed: (i) A 1D numerical model provides an upper limit of the temperature, and (ii) a more realistic concept that includes the time response and horizontal transport of the 3D atmospheric system is considered. The high-altitude (exospheric) temperature for the case of $1 W m^{-2}$ calculated at steady state with a 1D model by Waite *et al.* (16) is 230,000 K, which is much higher than the observed H_3^+ temperature of 1000 to 1500 K (20). The molecular diffusion times just above the methane homopause where the maximum heating occurs are much longer than a Jovian day. Therefore, we can examine a zonally averaged heating rate, which leads to a reduction in the vertically integrated heat flux ($15 \text{ ergs cm}^{-2} \text{ s}^{-1}$) and a corresponding exospheric temperature of 3000 K. The vertical temperature profile for this zonally averaged case is shown in Fig. 3 along with an observationally constrained profile for a more typical aurora (19) (10 to 100 less than the extremely bright aurora of Figs. 1 and 2). The time-variable temperature profile is bounded by these two ex-

Table 2. Local and integrated emission and energy flux.

	I2	W1
Maximum local count (counts per pixel)	13.3	1.7
Maximum apparent emission rate Lyman bands and continuum (MR)	>3.6	0.46
Local energy flux ($W m^{-2}$)	>0.75	0.1
Total counts	18,100	5,400
Observed radiated power (H_2 bands) ($10^{12} W$)	1	0.3
Estimated precipitated power (electrons) ($10^{12} W$)	7	2

treme cases. The initial temperatures may have risen locally to over 100,000 K. One can speculate that transport subsequently redistributed the heat by means of advective processes. Finally, a high exospheric temperature of over 3000 K quite likely persisted for several hours at all auroral longitudes with infrared hot spot structures remaining over the initial zone of heating and significant winds generated as a result of the large energy input.

An additional consideration is the uncertainty in our knowledge of the spectrum of the incoming precipitating particles. The exospheric temperature result is quite sensitive to the low-energy portion of this spectrum because the precipitating particles deposit their energy at high altitudes (pressure levels of about 1 nbar) that are further removed from the hydrocarbon cooling layer. For example, for 215-eV electrons, energy influxes on the order of $100 \text{ ergs cm}^{-2} \text{ s}^{-1}$ produce exospheric temperatures of over $10^6 K$. At these temperatures, the at-

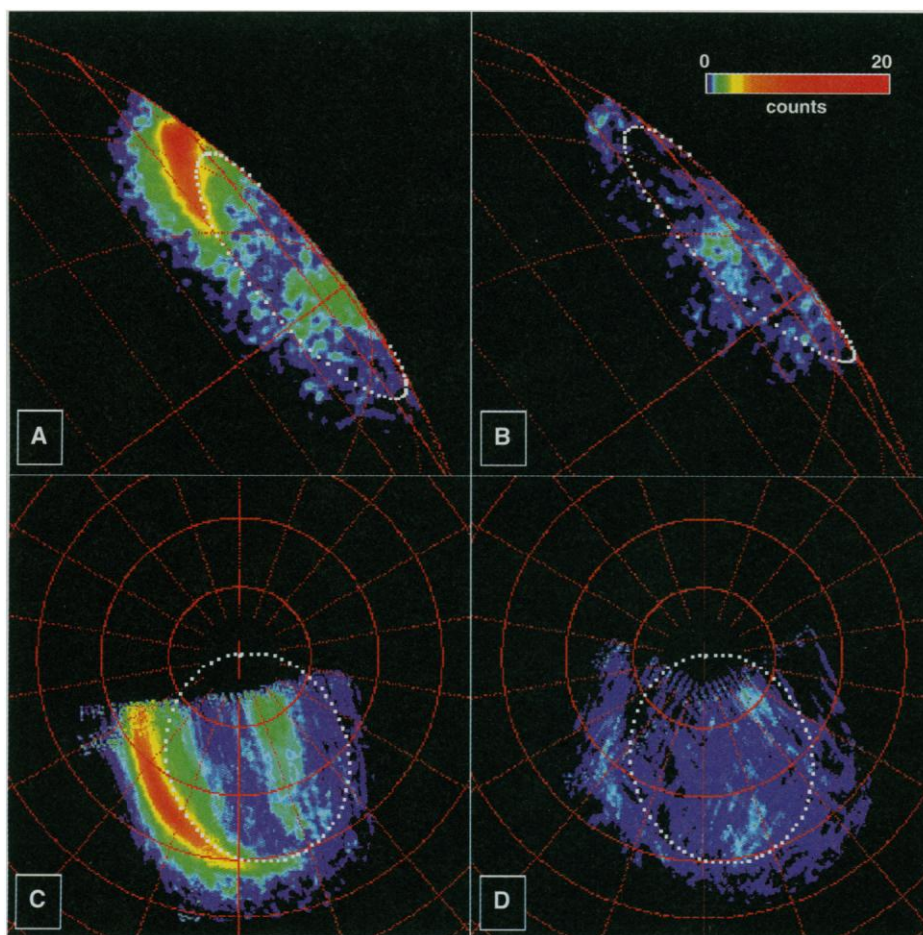


Fig. 2. (A and B) Background-subtracted version of the auroral images with a latitude-longitude grid coordinate (in red). Only features $\geq 1\sigma$ above the background are color-coded. Latitude parallels are separated by 10° and meridians increase by 20° from the lower right to the upper left. The white dots indicate the footprint of the $30-R_J$ field lines calculated from the Goddard Space Flight Center (GSFC) O_6 magnetic field model (27). (A) Exposure I2 showing an exceptionally bright aurora with a complex intensity distribution. (B) Exposure W1 showing a dramatic change in auroral brightness over the 19.5 hours since the observation in (A). (C and D) Polar projections of the two sets of bright and weak auroral images where data points $\geq 1\sigma$ above the disk background are considered. System III longitudes increase in 20° steps clockwise from the reference meridian ($\lambda_{III} = 0^\circ$), which is oriented toward the top. The 180° meridian is toward the bottom. (C) A composite of the bright images I1, I2, and I3, and (D) a combination of the weaker images W1, W2, and W3.

mosphere is no longer in hydrostatic equilibrium and literally blows off, creating a hydrogen corona. A very high temperature may help explain the highly Doppler-broadened Lyman α profiles that have been observed by IUE and more recently by HST (21). They may also explain why the aurora seems to often occur near the homopause level rather than in the thermosphere (where cooling by hydrocarbons is negligible), particularly at its brightest intensity (22). Indeed, the only stable situation in the case of energy input over $50 \text{ ergs cm}^{-2} \text{ s}^{-1}$ is when the altitude of the heating and cooling rates nearly coincide.

In the case of the previous exceptional Jovian auroral event observed with IUE, it was demonstrated that the auroral enhancement coincided with the arrival at Jupiter of a solar density disturbance, identified as a

coronal mass ejection (5). Therefore, we searched for similar associations with the July 1993 event. The *Ulysses* spacecraft was at high heliographic latitude in July 1993, and the plasma data confirm that it was out of the streamer belt at the time of our observations (23). Therefore, the *Ulysses* data are not useful in determining the solar wind conditions at Jupiter during the event.

The characteristic time of the observed brightness variation was less than 20 hours. This factor, together with the auroral location at high latitudes ($30 R_J$), indicates that the origin of auroral particles is not directly connected to the Io plasma torus ($6 R_J$). Rather, they appear to originate from the more distant (middle) magnetosphere and may be linked to field-aligned currents, observed during the *Ulysses* encounter with the Jovian magnetosphere, associated with

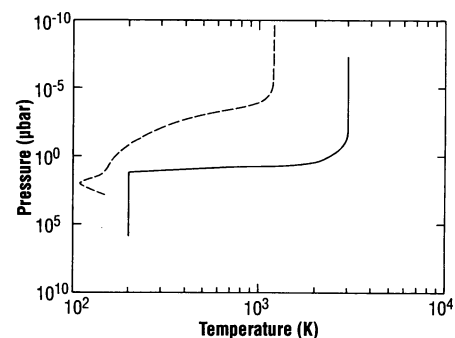


Fig. 3. Steady-state vertical distribution of the temperature of the Jovian auroral atmosphere calculated for electron precipitation with a 22-keV cutoff and for a total integrated heating rate of $15 \text{ ergs cm}^{-2} \text{ s}^{-1}$ (solid line). For comparison, the profile derived from observational spectroscopic constraints (20) is also shown (dotted line).

a high-latitude auroral arc observed at the Lyman α wavelength with the HST (24). It is interesting to compare the auroral processes at Jupiter with the better documented and understood terrestrial counterpart. The above arguments (high latitude, short time scale) suggest field-aligned current-driven auroral precipitations analogous to the terrestrial discrete aurora.

The strongly enhanced auroral emission reported here was observed on dayside field lines and was essentially fixed in magnetic longitude, not in local time. Longitudinally fixed auroral forms are consistent with the dominance of the corotational convective flow within the Jovian magnetosphere. In the inner magnetosphere ($< 20 R_J$), the plasma motion is dominated by the corotation electric field generated by the rapid rotation of the Jovian atmosphere-ionosphere. Outside of this distance ($20 R_J$), the plasma acceleration time becomes longer than the plasma outflow time. This suggests a decoupling of the ionosphere from the magnetosphere, that is, a departure from rigid corotation (25). This presents the possibility that reconnection processes near the magnetopause may produce localized solar wind convection cells in the outer magnetosphere, which may result in shears in the plasma flow near the plasma corotation boundary, in turn producing the field-aligned currents that are responsible for the high-latitude aurora. Evidence therefore suggests that auroral precipitations, similarly driven on Jupiter and the Earth by field-aligned currents, nevertheless originate from different mechanisms.

REFERENCES AND NOTES

1. A. L. Broadfoot *et al.*, *J. Geophys. Res.* **86**, 8259 (1981).
2. B. R. Sandel *et al.*, *Science* **206**, 962 (1979).
3. F. Herbert, B. R. Sandel, A. L. Broadfoot, *J. Geophys. Res.* **92**, 3141 (1987).
4. T. A. Livengood, H. W. Moos, G. E. Ballester, R.

Prangé, *Icarus* **97**, 26 (1992).

5. R. Prangé *et al.*, *J. Geophys. Res.* **98**, 18779 (1993).
6. J. C. Gérard, V. Dols, F. Paresce, R. Prangé, *ibid.*, p. 18793.
7. The overall sensitivity of the optical system is 4.1×10^{-6} counts per pixel per second for every kilorayleigh of H_2 Lyman emission. These observations were made before the addition of the Corrective Optics Space Telescope Axial Replacement (COSTAR), so the aberration of the HST primary mirror spread the light of a point source over a circular halo 2 arc sec in radius. All exposures (896 s each) described here were made with the use of the same guide star for telescope pointing and tracking. The center of the camera field of view was located along the planet's central meridian at $60^\circ N$ during each image.
8. F. W. Harris, personal communication.
9. The precise location of the planetary limb in the FOC field of view was determined from both the near-UV exposure (Table 1), which shows no auroral emission, and from the well-defined limb on each 153-nm auroral image.
10. V. Dols, J. C. Gérard, F. Paresce, R. Prangé, A. Vidal-Madjar, *Geophys. Res. Lett.* **19**, 1803 (1992).
11. The bulk of the H_2 Lyman emissions are emitted in bands near 160 and 161 nm and are optically thin in H_2 . Because the northern auroral oval is offset from the rotational pole, the effect of the slant path brightening is reduced somewhat by smearing during the exposure. During a typical exposure of 15 min, the planet rotates by about 9° of longitude. The slant path enhancement is also reduced if the actual auroral structure is unresolved by the FOC. A resolution of about 0.1 arc sec implies that structures smaller than about 400 km are diluted. For comparison, the scale height near the homopause on Jupiter is likely to be about 100 km or so, and a degree of latitude at $60^\circ N$ subtends about 600 km. We assumed that the aurora's vertical emission rate can be represented by a Chapman profile, used the nominal value of 100 km for the atmospheric scale height and an auroral height of 500 km above the cloud tops, and accounted for the dilution caused by the spatial resolution of the FOC (but not for smearing from the rotation of Jupiter).
12. J. C. Gérard, V. Dols, R. Prangé, F. Paresce, *Planet. Space Sci.*, in press.
13. J. Caldwell, B. Turgeon, X.-M. Hua, *Science* **257**, 1512 (1992).
14. This value can be considered as a lower limit because the aberrated point spread function of the telescope and the blurring effect of the planetary rotation spreads the light of a point source over many pixels and decreases the apparent emission rate of localized emission. A rough estimate of this effect may be obtained from the deconvolved (Wiener) version of Fig. 2A, although this method does not necessarily provide correct photometric values. The brightest region in this case reaches ~ 10 MR of H_2 Lyman emission.
15. J. C. Gérard and V. Singh, *J. Geophys. Res.* **87**, 4525 (1982).
16. H. J. Waite *et al.*, *ibid.* **88**, 6143 (1983).
17. D. Rego, R. Prangé, J. C. Gérard, *ibid.* **99**, 17075 (1994).
18. The results of the 1 W m^{-2} aurora excited by electrons with the Ulysses energy spectrum imply an H_2^+ production rate exceeding $2 \times 10^6 \text{ cm}^{-3}$ with a peak production expected near the $1\text{-}\mu\text{bar}$ pressure level and a peak H_3^+ density on the order of 10^8 cm^{-3} . The corresponding heating rate also peaks at this pressure with a vertically integrated heat flux of over $450 \text{ ergs cm}^{-2} \text{ s}^{-1}$. The heating rate profile calculated from the model can be combined with recent cooling rate calculations (scaled so that the vertically integrated cooling rate equals the vertically integrated heating rate and peaks at a pressure level of $1 \mu\text{bar}$, just above the methane homopause, that is, cool-to-space approximation). These values were used as inputs in a 1D thermal conduction equation (26) to estimate the auroral thermal profile.
19. L. M. Trafton, J. C. Gérard, G. Munhoven, J. H. Waite, *Astrophys. J.* **421**, 816 (1994).
20. P. Drossart *et al.*, *J. Geophys. Res.* **98**, 18803 (1993).
21. J. T. Clarke *et al.*, *Astrophys. J. Lett.* **430**, 73 (1994).

22. G. R. Gladstone and T. Skinner, *NASA SP-494* (1989), pp. 221–228.
23. M. Hammond and J. Gosling, personal communication.
24. M. K. Dougherty, D. J. Southwood, A. Balogh, E. J. Smith, *Planet. Space Sci.* **41**, 291 (1993); R. Prangé, M. Dougherty, M. Dunlop, A. Balogh, V. Dols, *Eos* **74**, 43 (1993).
25. V. Vasyliunas, *Geophys. Res. Lett.* **21**, 401 (1994).
26. H. J. Waite, M. L. Chandler, R. V. Yelle, B. R. Sandel, T. E. Cravens, *J. Geophys. Res.* **93**, 14295 (1988).
27. J. E. P. Connerney, in *Planetary Radio Emission III*, H. Rucker, M. L. Kaiser, S. J. Bauer, Eds. (Austrian Academy of Sciences Press, Vienna, 1992), pp. 13–33.
28. J.C.G. acknowledges support from the Belgian National Fund for Scientific Research (FNRS) and

from the Belgian Federal Science Policy Office, Prime Minister's Services. R.P. is grateful to J. Gosling, M. Hammond, K. Maeda, H. Oya, and P. Zarka for fruitful discussions and for having kindly provided unpublished data on the Jovian radio emission and on the solar wind. She acknowledges partial support of this study by grant INSU-PNP/80374200. J.H.W. acknowledges support from Space Telescope Science Institute grant GO-4608.02-92A and National Aeronautics and Space Administration (NASA) Planetary Atmosphere grant NAGW-3624. This study is based on observations with the NASA-ESA HST that were obtained at the Space Telescope Science Institute, which is operated by AURA for NASA under contract NAS5-26555.

11 July 1994; accepted 27 September 1994

In Situ Determination of the NiAs Phase of FeO at High Pressure and Temperature

Yingwei Fei and Ho-kwang Mao

In situ synchrotron x-ray diffraction measurements of FeO at high pressures and high temperatures revealed that the high-pressure phase of FeO has the NiAs structure (B8). The lattice parameters of this NiAs phase at 96 gigapascals and 800 kelvin are $a = 2.574(2)$ angstroms and $c = 5.172(4)$ angstroms (the number in parentheses is the error in the last digit). Metallic behavior of the high-pressure phase is consistent with a covalently and metallicity bonded NiAs structure of FeO. Transition to the NiAs structure of FeO would enhance oxygen solubility in molten iron. This transition thus provides a physicochemical basis for the incorporation of oxygen into the Earth's core.

Ferrous oxide is a basic oxide component in the interior of the Earth. Its high-pressure and high-temperature behavior plays an important role in mantle composition and core formation models. Since shock wave studies (1) revealed the existence of a high-pressure phase of FeO at pressures above 70 GPa over a decade ago, the structure of this phase has been the subject of speculation (1–4). Transition to this phase has not been observed in static compression experiments in the diamond-anvil cell up to 120 GPa at room temperature (5). Additional shock compression experiments (6) have confirmed that the density of FeO changes at 70 GPa. The discrepancy between the static and shock compression experiments may be related to the experimental temperature difference in the two techniques. In this study, we report static high-pressure and high-temperature experiments on FeO that resolve this discrepancy. In addition, in situ synchrotron x-ray measurements reveal the structure of the high-pressure, high-temperature phase of FeO. We discuss implications of the high-pressure structure of FeO for the incorporation of oxygen (in the form of FeO) into the Earth's core and for the mineralogy of the lower mantle.

We have developed an externally heated

Geophysical Laboratory and Center for High-Pressure Research, 5251 Broad Branch Road, N.W., Washington, DC 20015, USA.

high-temperature diamond-anvil cell (7, 8) that is capable of achieving pressures greater than 125 GPa at temperatures up to 1100 K in a mildly reducing atmosphere (Ar with 1% H_2). We conducted experiments on FeO by using this high-temperature cell combined with in situ synchrotron x-ray diffraction measurements. At room temperature, we confirmed the transition from the cubic (B1) to a rhombohedral phase at 16 GPa under hydrostatic conditions (5) (Fig. 1). The transition occurs at much lower pressure (~ 8 GPa) when no pressure medium is used in the experiments. High-temperature and high-pressure experiments, carried out in neon pressure medium, show that the transition boundary has a positive pressure-temperature slope with $P = -5.0 + 0.070T$ (for pressure in gigapascals and temperature in kelvin).

At higher pressure, we carried out two experiments on FeO without a pressure medium. The two experiments were identical in experimental configuration but different in the pressure and temperature ranges. We observed no phase transition between 16 and 84 GPa at room temperature, consistent with previous static compression experiments (5). Upon heating, new diffraction peaks started to appear at 74 GPa and 900 K in the first experiment and at 90 GPa and 600 K in the second experiment. In the first experiment, the diffraction peaks from the new phase became more intense with